Theory of coherent Raman superradiance imaging of condensed Bose gases

H. Uys and P. Meystre

Department of Physics, The University of Arizona, Tucson, Arizona 85721, USA

We describe theoretically the dynamics of the off-resonant superradiant Raman scattering of light in a prolate atomic Bose-Einstein condensate, from the initial stages governed by quantum fluctuations to the subsequent semiclassical regime, and within a multimode theory that fully accounts for propagation effects. Our results are in good agreement with recent experimental results that exploit Raman superradiance as an imaging technique to probe the long-range coherence of condensates, including the observed time-dependent spatial features, and account properly for the macroscopic shot-to-shot fluctuations resulting from the quantum noise that initiates the superradiance process.

I. INTRODUCTION

In a beautiful recent series of experiments, Sadler and co-workers have exploited superradiant Raman scattering as a probe of long-range coherence in a quantum-degenerate bosonic gas [1]. Their investigation is one of few experimental studies of extended sample superradiance that is both temporally and spatially resolved. The detailed information that can be extracted from such experiments provides a strong motivation to revisit the theory of superradiance and to bring it to a level of sophistication at a par with these developments.

Superradiance is a well-known phenomenon [2] that was discussed by Dicke [3] in 1954. In that process, atoms scatter light collectively, producing a short burst of intense radiation. In a typical superradiance experiment with Bose-Einstein condensates, an elongated sample of ultracold atoms is subjected to a pump pulse of far off-resonant laser light. For an appropriate polarization of that field, the condensate geometry results in the scattering of photons predominantly into modes propagating along the long axis of the sample, commonly referred to as the end-fire modes (EFM). As the atomic cloud is Bose condensed, the scattering process simultaneously leads to the coherent amplification of the recoiling atomic fields. Such coherent matter-wave amplification (CMA) has been observed both in the case of Rayleigh scattering [4–6] and of Raman scattering [7,8], and several theoretical descriptions of this effect have been published [9–12].

A necessary condition for superradiance to occur is [13–15]

$$\tau_c \ll T_2^*, \tag{1}$$

where T_2^* is the reciprocal inhomogeneous linewidth and $\tau_c = 2/(c\rho\gamma\lambda^2)^{1/2}$ is the superradiant cooperation time with ρ the atomic density, c the speed of light, λ the transition wavelength, and γ the linewidth of an isolated atom.

An ultracold bosonic gas at temperature T with $0 < T < T_c$, where T_c is the critical temperature, consists of both condensed and noncondensed phases. As Doppler broadening for the two phases can be dramatically different, it is possible for the appropriate choice of experimental parameters to have condition Eq. (1) satisfied for the condensed

phase, but not the noncondensed phase [4]. Under such circumstances light will scatter superradiantly only from the condensed portion of the gas, thus providing the experimenter with a sensitive probe of that phase. In Ref. [1] this approach is followed to both quantify the condensate number and study the spatial and temporal evolution of the superradiant process. It provides a probe of long-range coherence, which may lead to insight in the symmetry-breaking dynamics of normal-to-superfluid phase transitions. To our knowledge only one previous experimental study [4] exists that resolves spatial features in extended sample superradiance in atomic vapors. In that case the angular pattern of the emitted EFM was integrated over the course of a superradiant pulse and found to consist of several bright spots [Fig. 3(a) in Ref. [4]].

Zobay and Nikolopoulos [16,17] have given a detailed semiclassical analysis of the spatial features of both the matter-wave and the optical fields in CMA experiments based on Rayleigh scattering. They found that propagation effects play a crucial role in the amplification process and account for several characteristic features seen in experiments [4,7]. These include the characteristic X and fan shapes of the atomic recoil modes corresponding to the strong and weak pulse limits, respectively, the asymmetry between forward and backward side modes in the strong pulse regime, and the depletion of the condensate center in the weak pulse regime. Furthermore, they found that low superradiant emission does not necessarily imply a small EFM field inside the atomic sample, as a result of the scattering of EFM photons back into the pump beam. They also demonstrated that propagation effects lead to subexponential growth of the scattered fields in contrast to the exponential growth seen in fully quantized uniform field models, an effect reminiscent of laser lethargy in short-wavelength optical amplifiers [18,19].

An important aspect of superradiance experiments is the appearance of large shot-to-shot fluctuations, a result of the quantum noise that dominates the dynamics during the initial stages of the experiment [2,20–22]. At later times the scattered fields become macroscopically occupied and evolve in an essentially classical manner from initial conditions determined by those quantum fluctuations. A common strategy to treat the full evolution of superradiance is therefore to break the problem into an initial quantum stage followed by a clas-

sical stage. The initial stage is analyzed primarily to determine the appropriate probability distribution of initial conditions for the classical stage. Experimentally observed fluctuations in the classical stage are simulated by solving the dynamics a large number of times with initial conditions chosen according to this probability distribution, each simulation representing a single realization of the experiment.

A primary aim of this paper is to provide a detailed theoretical framework to interpret experiments such as reported in Ref. [1]. With this goal in mind we generalize the semiclassical model of Refs. [16,17] to the Raman scattering case, and also extend it to a multimode quantum description that allows for a systematic treatment of the buildup of the classical fields from quantum noise, thereby accounting for shot-to-shot fluctuations. Whereas Refs. [16,17] focus on the post-pump expansion patterns of the recoiling modes, we also investigate in detail the time-dependent imaging of the condensate *while* undergoing superradiant emission and find good qualitative agreement with experimental observations. The present theory is limited to the zero-temperature limit and to the case of bosonic atoms, but these limitations will be removed in future work.

We note that although superradiance imaging can work in principle both for Raman and Rayleigh transitions, Raman superradiance offers several distinct advantages. Most importantly perhaps, in Raman superradiance the atoms are not further scattered to higher-order spatial modes after having been scattered once, making the interpretation of the experiments significantly simpler than in the case of Rayleigh scattering. Also, Raman superradiance differs from Rayleigh superradiance in that in the former case, the physical mechanism at the origin of the process is the creation of a spin polarization grating in the sample, while it is a density grating in the latter situation, thereby eliminating the dispersive phase shift that would cause aberrations in imaging (see Ref. [1]).

The paper is organized as follows. Section II discusses the experiment under consideration, introduces our model, and considers the initial stages of the evolution of the atoms and light field, treating the scattered optical field quantum mechanically. Section III turns then to the classical stage by solving coupled Maxwell-Schrödinger equations within the slowly varying envelope approximation. Numerical results are presented in Sec. IV, and Sec. V is a summary and conclusion.

II. INITIAL STAGE AND QUANTUM FLUCTUATIONS

We consider a cigar-shaped Bose-Einstein condensate of width w and length L with a total of N atoms. The ultracold atoms in the condensate undergo Raman scattering between two ground states $|1\rangle$ and $|2\rangle$ via an off-resonant excited state $|e\rangle$. The energy of level $|1\rangle$ is taken as the zero of energy, and the energies of the states $|2\rangle$ and $|e\rangle$ are $\hbar\omega_2$ and $\hbar\omega_e$, respectively (see Fig. 1). We assume that the transition $|1\rangle \rightarrow |e\rangle$ is driven by a classical pump laser $\mathbf{E}_L(t)$ of frequency ω_L and polarized along the $\hat{y}$ axis (see Fig. 2), with

$$\delta_L = \omega_e - \omega_L, \quad (2)$$

while the transition $|e\rangle \rightarrow |2\rangle$ takes place via spontaneous emission to a continuum of vacuum modes with frequencies
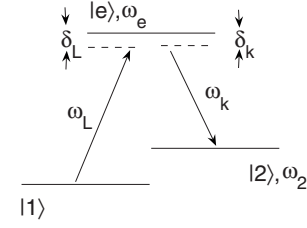
FIG. 1. Three-level Raman transition.

$$\omega_k = \omega_e - \omega_2 - \delta_k. \quad (3)$$

The total electric field is then

$$\hat{\mathbf{E}} = \mathbf{E}_L(t) + \sum_{\hat{\boldsymbol{\epsilon}}} \int d\mathbf{k}\, \hat{\mathbf{E}}_{\mathbf{k}}$$

$$= \hat{\mathbf{y}}[E_L(t)e^{i(\mathbf{k}_L \cdot \mathbf{r} - \omega_L t)} + E_L^*(t)e^{-i(\mathbf{k}_L \cdot \mathbf{r} - \omega_L t)}]$$

$$+ \sum_{\hat{\boldsymbol{\epsilon}}} \int d\mathbf{k} \left[\left(\frac{\hbar\omega_{\mathbf{k}}}{2\epsilon_0 V}\right)^{1/2} \hat{\boldsymbol{\epsilon}}_{\mathbf{k}} \hat{a}_{\hat{\boldsymbol{\epsilon}}\mathbf{k}}(t) e^{i\mathbf{k}\cdot\mathbf{r}} + \text{H.c.} \right],$$

where the creation operators $\hat{a}_{\hat{\boldsymbol{\epsilon}}\mathbf{k}}^{\dagger}(t)$ obey the usual bosonic commutation relations

$$[\hat{a}_{\hat{\boldsymbol{\epsilon}}\mathbf{k}}, \hat{a}_{\hat{\boldsymbol{\epsilon}}'\mathbf{k}'}^{\dagger}] = \delta(\mathbf{k} - \mathbf{k}')\delta_{\hat{\boldsymbol{\epsilon}}\hat{\boldsymbol{\epsilon}}'}. \quad (4)$$

The incident laser-field envelope $E_L(t)$ is taken as constant in amplitude during the initial stages of the amplification process, but its full-time dependence can be accounted for in the classical stages of the evolution.

We proceed by introducing bosonic matter-field creation and annihilation operators $\hat{\psi}_i^{\dagger}(\mathbf{r},t)$ $[\hat{\psi}_i(\mathbf{r},t)]$, that create (annihilate) an atom at position $\mathbf{r}$ in electronic state $|i\rangle = |1\rangle, |e\rangle$, or $|2\rangle$, with

$$[\hat{\psi}_i(\mathbf{r},t), \hat{\psi}_j^{\dagger}(\mathbf{r}',t)] = \delta_{ij}\delta(\mathbf{r} - \mathbf{r}'), \quad (5)$$

in terms of which the Hamiltonian of the atom-field system is $\hat{H} = \hat{H}_0 + \hat{H}_c$, with

$$\hat{H}_0 = \sum_{\hat{\boldsymbol{\epsilon}}} \int d\mathbf{k}\hbar\omega(\mathbf{k})\hat{a}_{\hat{\boldsymbol{\epsilon}}\mathbf{k}}^{\dagger}(t)\hat{a}_{\hat{\boldsymbol{\epsilon}}\mathbf{k}}(t) + \int d\mathbf{r}\{\hbar\omega_e\hat{\psi}_e^{\dagger}(\mathbf{r},t)\hat{\psi}_e(\mathbf{r},t)$$

$$+ \hbar\omega_2\hat{\psi}_2^{\dagger}(\mathbf{r},t)\hat{\psi}_2(\mathbf{r},t)\}, \quad (6)$$

and the interaction Hamiltonian
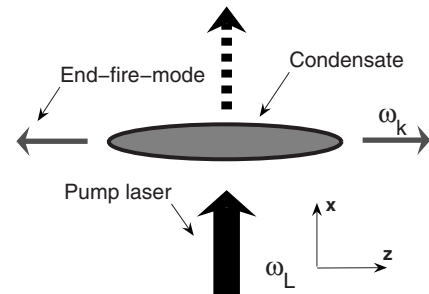
FIG. 2. Experimental setup.

$$\hat{H}_c = -\int d\mathbf{r}\{\hat{\mathbf{E}}\cdot[\mathbf{d}_1\hat{\psi}_e^\dagger(\mathbf{r},t)\hat{\psi}_1(\mathbf{r},t) + \mathbf{d}_2\hat{\psi}_e^\dagger(\mathbf{r},t)\hat{\psi}_2(\mathbf{r},t)]$$
$$+ \text{H.c.}\}, \tag{7}$$

describes the electric-dipole interaction between the atoms and the electromagnetic field, $\mathbf{d}_i$ being the dipole moment of the $|i\rangle \leftrightarrow |e\rangle$ transition.

We assume that the atoms are initially in their ground state $|1\rangle$, and that the pump laser is sufficiently far detuned from resonance for the excited-state population to remain negligible at all times. The excited level $|e\rangle$ can then be adiabatically eliminated in the standard fashion. Thus transforming to slowly varying interaction picture operators

$$\tilde{a}_{\hat{\epsilon}\mathbf{k}}(\mathbf{r},t) = \hat{a}_{\hat{\epsilon}\mathbf{k}}e^{i\omega_L t}, \tag{8}$$

$$\tilde{\psi}_1(\mathbf{r},t) = \hat{\psi}_1(\mathbf{r},t), \tag{9}$$

$$\tilde{\psi}_e(\mathbf{r},t) = \hat{\psi}_e(\mathbf{r},t)e^{i\omega_e t}, \tag{10}$$

$$\tilde{\psi}_2(\mathbf{r},t) = \hat{\psi}_2(\mathbf{r},t)e^{i\omega_2 t}, \tag{11}$$

and performing the rotating-wave approximation (RWA), yields the effective Hamiltonian

$$\tilde{H}_c = -\int d\mathbf{r}\int d\mathbf{k}\{g(\mathbf{k})\tilde{a}_{\hat{\epsilon}\mathbf{k}}^\dagger\tilde{\psi}_2^\dagger(\mathbf{r},t)e^{i(\mathbf{k}_L-\mathbf{k})\cdot\mathbf{r}}\tilde{\psi}_1(\mathbf{r},t)e^{i(\delta_L-\delta_k)t}$$
$$+ \text{H.c.}\}, \tag{12}$$

where

$$g(\mathbf{k}) = (\hat{\mathbf{y}}\cdot\mathbf{d}_1)(\hat{\epsilon}\cdot\mathbf{d}_2)\sqrt{\frac{\omega_k}{2\hbar\epsilon_0 V}}\left(\frac{\delta_k+\delta_L}{\delta_k\delta_L}\right)E_L. \tag{13}$$

In Eq. (12) we have neglected scattering processes that do not involve the incident laser.

The effect of the Hamiltonian $\tilde{H}$ is to transfer atoms initially in the ground state $|1\rangle$ and with spatial wave function $\phi_0(\mathbf{r})$ into the ground state $|2\rangle$ with a momentum-conserving spatial wave function $\phi_0(\mathbf{r})e^{i(\mathbf{k}_L-\mathbf{k})\cdot\mathbf{r}}$ via scattering of a photon into mode $\mathbf{k}$, hereby creating a spin-polarization grating in the medium. Following Ref. [10] we therefore expand the matter-field operators into quasimodes according to

$$\tilde{\psi}_1(\mathbf{r}) = \phi_0(\mathbf{r})\tilde{c}_0, \tag{14}$$

and

$$\tilde{\psi}_2(\mathbf{r}) = \int d\mathbf{q}\,\phi_0(\mathbf{r})e^{i\mathbf{q}\cdot\mathbf{r}}\tilde{c}_q, \tag{15}$$

where $\tilde{c}_0$ annihilates a particle in a quasimode with electronic state $|1\rangle$ and wave function $\langle\mathbf{r}|0\rangle = \phi_0(\mathbf{r})$ and $\tilde{c}_q$ annihilates a particle in a quasimode with electronic state $|2\rangle$ and wave function $\langle\mathbf{r}|\mathbf{q}\rangle = \phi_0(\mathbf{r})e^{i\mathbf{q}\cdot\mathbf{r}}$. These quasimodes are nearly orthogonal provided that they are separated by an angle

$$\theta_\perp \gtrsim 2K_w/|k| = \lambda_L/(\pi w),$$

where $\lambda_L = 2\pi c/\omega_L$ and $K_w = 2/w$ is the momentum width of the condensate. In that case the quasimode creation and an-

nihilation operators $\tilde{c}_q$ obey to a good approximation bosonic commutation relations

$$[\tilde{c}_q,\tilde{c}_{q'}^\dagger] \approx \delta_{qq'}, \tag{16}$$

and are statistically independent during the early stages of the evolution.

In terms of the quasimodes q, the Hamiltonian (12) becomes

$$H_c = \sum_q \int d\mathbf{k}\{\eta(\mathbf{k},q)e^{i(\delta_L-\delta_k)t}\tilde{a}_\mathbf{k}^\dagger\hat{c}_q^\dagger\hat{c}_0 + \text{H.c.}\}, \tag{17}$$

where

$$\eta_\mathbf{q}(\mathbf{k}) = g(\mathbf{k})\int d\mathbf{r}|\phi_0(\mathbf{r})|^2 e^{i(\mathbf{k}_L-\mathbf{k}-\mathbf{q})\cdot\mathbf{r}}. \tag{18}$$

We have used the normalization condition $\int d\mathbf{r}|\phi_0(\mathbf{r})|^2 = 1$. The Hamiltonian (17) differs from the effective Hamiltonian derived by Moore and Meystre for the Rayleigh scattering case [10] in that the electronic state of recoiling atomic modes is $|2\rangle$ instead of the original ground state $|1\rangle$ and the term oscillating with frequency $\delta_L-\delta_k = \omega_k-(\omega_L-\omega_2)$ enforces the coupling of the scattered modes to photons with frequency $\omega_L-\omega_2$ instead of ω_L.

With these differences in mind, we may easily generalize the results of Ref. [10] and determine that the quasimodes initially grow exponentially,

$$\tilde{c}_\mathbf{q} = \exp[G_\mathbf{q}Nt/2]\tilde{c}_\mathbf{q}(0) + \int_0^t d\tau\exp[G_\mathbf{q}Nt/2]\tilde{f}_\mathbf{q}^\dagger(t-\tau), \tag{19}$$

where

$$G_\mathbf{q} = 2\pi\int d\mathbf{k}|\eta_\mathbf{q}(\mathbf{k})|^2\delta(\omega_k-(\omega_L-\omega_2)), \tag{20}$$

and $\tilde{f}_\mathbf{q}(t-\tau)$ is a noise operator the second-order correlation functions of which are given in the Markov approximation by

$$\langle\tilde{f}_\mathbf{q}^\dagger(t)\tilde{f}_\mathbf{q}(t')\rangle = 0, \tag{21}$$

$$\langle\tilde{f}_\mathbf{q}(t)\tilde{f}_\mathbf{q}^\dagger(t')\rangle = G_\mathbf{q}N\delta(t-t'). \tag{22}$$

In this limit, the probability $P_\mathbf{q}(n,t)$ of having n atoms in mode $\mathbf{q}$ at time t is that of a chaotic field,

$$P_\mathbf{q}(n,t) = \frac{1}{\bar{n}_\mathbf{q}(t)}\left(1+\frac{1}{\bar{n}_\mathbf{q}(t)}\right)^{-(n+1)}, \tag{23}$$

where $\bar{n}_\mathbf{q}(t) = \langle\tilde{c}_\mathbf{q}^\dagger\tilde{c}_\mathbf{q}\rangle$ is the mean number of atoms in the quasimode q at time t.

An important feature of the linear gain factor $G_\mathbf{q}$ is that it remains relatively constant for quasimodes excited via the scattering of photons at small angles $\theta_\mathbf{k}$ with respect to the long axis of the condensate. This is the case until $\theta_\mathbf{k}$ reaches the geometric angle

$$\theta_g \approx \frac{w}{L},$$

after which the linear gain $G_{\mathbf{q}}$ falls off rapidly. The electromagnetic modes corresponding to scattering into that angle collectively form the EFMs, and they dominate the short-time dynamics of the system.

This suggests that we may accurately simulate the linear dynamics of the superradiant system by considering the scattering of photons into a finite number of modes distributed within a solid angle $2\pi\theta_g$ around the long axis of the condensate only. We note that while the geometric angle into which significant scattering takes place is fixed by the aspect ratio of the condensate, the number m of independent quasi-modes depends also on the wavelength of the optical fields involved,

$$m \approx \left(\frac{\theta_g}{\theta_\perp}\right)^2 = \left(\frac{\pi w^2}{2\lambda_L L}\right)^2 = F^2, \tag{24}$$

where F is the Fresnel number. Typical experiments correspond to a number of quasimodes $m \approx 1-10^2$.

III. CLASSICAL EVOLUTION

We now turn to the quantum-noise-initiated classical regime that occurs once the superradiance process is fully under way and the scattered modes are macroscopically occupied. In typical experiments of Ref. [1] the velocity of the recoiling atoms is such that they may traverse half a condensate width over the course of a single run of the experiment. In addition, atom-atom scattering may cause significant dephasing on the same time scale. In this section we therefore include both kinetic energy and mean-field atom-atom collisional terms.

In the classical regime the optical field can be described by a complex field amplitude,

$$\begin{aligned} \mathbf{E}_{cl} &= \mathbf{E}_L + \sum_{\mathbf{k}} \mathbf{E}_{\mathbf{k}} \\ &= \hat{\mathbf{y}}[E_L(\mathbf{r},t)e^{i(\mathbf{k}_L\cdot\mathbf{r}-\omega_L t)} + E_L^*(\mathbf{r},t)e^{-i(\mathbf{k}_L\cdot\mathbf{r}-\omega_L t)}] \\ &\quad + \sum_{\hat{\mathbf{e}}\mathbf{k}} \hat{\mathbf{e}}[E_{\mathbf{k}}(\mathbf{r},t)e^{i(\mathbf{k}\cdot\mathbf{r}-\omega_k t)} + E_{\mathbf{k}}^*(\mathbf{r},t)e^{-i(\mathbf{k}\cdot\mathbf{r}-\omega_k t)}]. \end{aligned}$$

Following the discussion of Sec. II we restrict the sum over $\mathbf{k}$ to the discrete set of quasimodes in the end-fire cone and set $\omega_k = \omega_L - \omega_2$. At this point we no longer assume that the pump field remains undepleted. As usual, the field amplitudes $E_i(\mathbf{r},t)$ are assumed to be slowly varying,

$$|\boldsymbol{\nabla} E_i(\mathbf{r},t)| \ll |k_i E_i(\mathbf{r},t)|, \tag{25}$$

$$\left|\frac{\partial E_i(\mathbf{r},t)}{\partial t}\right| \ll |\omega_i E_i(\mathbf{r},t)|. \tag{26}$$

Eliminating adiabatically the excited electronic state of the atoms as before by introducing the slowly varying Schrödinger-field operators

$$\tilde{\psi}_0(\mathbf{r},t) = \hat{\psi}_1(\mathbf{r},t), \tag{27}$$

$$\tilde{\psi}_{\mathbf{k}_L}(\mathbf{r},t) = \hat{\psi}_e(\mathbf{r},t)e^{i(\omega_e+\omega_{er})t}e^{-i\mathbf{k}_L\cdot\mathbf{r}}, \tag{28}$$

$$\tilde{\psi}_{\mathbf{k}}(\mathbf{r},t) = \hat{\psi}_{\mathbf{k}}(\mathbf{r},t)e^{i(\omega_2+\omega_{2r})t}e^{-i(\mathbf{k}_L\cdot\mathbf{r}-\mathbf{k}\cdot\mathbf{r})}, \tag{29}$$

where $\hbar\omega_{er}=\hbar^2 k_L^2/2m$ and $\hbar\omega_{2r}=\hbar^2(k_L^2+k^2)/2m$, results in the effective Hamiltonian $\tilde{H}=\tilde{H}_0+\tilde{H}_{aa}+\tilde{H}_c$, where

$$\tilde{H}_0 = -\int d\mathbf{r}\left\{\sum_{\mathbf{k}} \frac{\hbar^2}{2m}\tilde{\psi}_{\mathbf{k}}^\dagger\nabla^2\tilde{\psi}_{\mathbf{k}}\right\}, \tag{30}$$

$$\begin{aligned} \tilde{H}_{aa} = -\int d\mathbf{r}\bigg\{ &U_{11}\tilde{\psi}_0^\dagger\tilde{\psi}_0^\dagger\tilde{\psi}_0\tilde{\psi}_0 + \sum_{\mathbf{k}}(U_{kk}\tilde{\psi}_{\mathbf{k}}^\dagger\tilde{\psi}_{\mathbf{k}}^\dagger\tilde{\psi}_{\mathbf{k}}\tilde{\psi}_{\mathbf{k}} \\ &+ U_{1k}\tilde{\psi}_0^\dagger\tilde{\psi}_{\mathbf{k}}^\dagger\tilde{\psi}_{\mathbf{k}}\tilde{\psi}_0)\bigg\}, \end{aligned} \tag{31}$$

$$\tilde{H}_c = -\int d\mathbf{r}\sum_{ij} \frac{g_{ij}}{(1-i\gamma/\delta_L)}\tilde{\psi}_i^\dagger(\mathbf{r},t)\tilde{\psi}_j(\mathbf{r},t). \tag{32}$$

Here

$$g_{ij} = \frac{d_i d_j}{3\delta_L\hbar}E_i^*(\mathbf{r},t)E_j(\mathbf{r},t), \tag{33}$$

in which the factor 3 arises from an average over all possible orientations of the dipole and

$$U_{11(kk)} = \frac{4\pi\hbar^2 a}{m}, \quad U_{1k} = \frac{8\pi\hbar^2}{m}(a+ika^2), \tag{34}$$

where a is the s-wave scattering length and the indices i,j run over $-k,0,k$. The last term on the right in Eq. (34) is a momentum-dependent loss that has been used to account for elastic-scattering losses in the Gross-Pitaevskii equation [23]. It arises upon keeping the second-order term when expanding the many-body T matrix in powers of k. For the Raman system under consideration we need not include higher-order modes of the form $\tilde{\psi}_{n\mathbf{k}_L+q\mathbf{k}}$ (n,q being integers) in the sum over $\mathbf{k}$, since the second ground state can no longer absorb pump photons [7].

Within the slowly varying envelope approximation (SVEA) the Hamiltonian (32) yields the matter-wave Heisenberg equations of motion

$$\begin{aligned} \frac{d\Psi_0(\mathbf{r},t)}{d\tau} = &\frac{i}{(1-i\gamma/\delta_L)}\mathcal{E}_L^*\left[\frac{d_1}{d_2}\mathcal{E}_L\Psi_0 + \sum_{\mathbf{k}}\mathcal{E}_{\mathbf{k}}\Psi_{-\mathbf{k}}\right] \\ &+ i\sum_j u_{1j}|\Psi_j|^2\Psi_0, \end{aligned} \tag{35}$$

$$\begin{aligned} \frac{d\Psi_{\mathbf{k}}(\mathbf{r},t)}{d\tau} = &-\boldsymbol{\kappa}\cdot\boldsymbol{\nabla}\Psi_{\mathbf{k}} + \frac{i}{(1-i\gamma/\delta_L)}\mathcal{E}_{-\mathbf{k}}^*\bigg[\mathcal{E}_L\Psi_0 \\ &+ \frac{d_2}{d_1}\sum_{\mathbf{k}}\mathcal{E}_{\mathbf{k}}\Psi_{-\mathbf{k}}\bigg] + i\sum_j u_{kj}|\Psi_j|^2\Psi_k. \end{aligned} \tag{36}$$

We have cast these equations in dimensionless units where the dimensionless time is

$$\tau = \frac{\Omega_L^2}{\delta_L} t, \tag{37}$$

in which

$$\Omega_L = \frac{d E_L^{\text{in}}}{\sqrt{3}\hbar} \tag{38}$$

is the Rabi frequency of the incident laser field of amplitude E_L^{in} and $d = \sqrt{d_1 d_2}$. The electric-field amplitudes are rescaled as

$$\mathcal{E}_i = \frac{E_i}{E_L^{\text{in}}}, \tag{39}$$

and the matter-wave fields as

$$\Psi_i = \frac{\widetilde{\psi}_i}{\sqrt{\rho_c}}, \tag{40}$$

where

$$\rho_c = \frac{N}{Lw^2} \tag{41}$$

is a characteristic density.

When performing the derivatives of the kinetic-energy term, dimensional analysis along with the SVEA indicate that the second-order derivative is smaller than the first by a factor of 10^{-4}. We have therefore retained only the advective contribution [first term on the right in Eq. (36)] with a dimensionless velocity

$$\boldsymbol{\kappa} = \frac{\delta_L}{L\Omega_L^2} \frac{\hbar}{2m} (\mathbf{k}_L + \mathbf{k}). \tag{42}$$

Finally, the rescaled atom-atom scattering strength is

$$u_{ij} = \frac{\delta_L}{\Omega_L^2} U_{ij}. \tag{43}$$

The recoil velocity imparted by the scattering process on the condensate atoms is of the order of centimeters per second. The resulting recoil motion of the scattered atoms through the original condensate is neglected in some of the simulations presented in Sec. IV, an excellent approximation for the early stages of the dynamics. The factor γ/δ_L in Eqs. (35) and (36) is due to the inclusion of a phenomenological decay term to account for losses due to spontaneous emission from the excited state.

The evolution of the optical field is governed by the Maxwell wave equation coupled to the macroscopic polarization of the condensate. Treating the pump laser as a continuous wave we find

$$\frac{\partial \mathcal{E}_L}{\partial \xi} = \frac{i\aleph}{(1 - i\gamma/\delta_L)} \Psi_0^{\dagger} \left\{ \frac{d_1}{d_2} \mathcal{E}_L \Psi_0 + \sum_k \mathcal{E}_k \Psi_{-k} \right\}, \tag{44}$$

$$\text{sgn}(k)\frac{\partial \mathcal{E}_k}{\partial \zeta} = \frac{i\aleph}{(1 - i\gamma/\delta_L)} \Psi_{-k}^{\dagger} \left\{ \mathcal{E}_L \Psi_0 + \frac{d_2}{d_1}\sum_k \mathcal{E}_k \Psi_{-k} \right\}, \tag{45}$$

where $\xi = x/L$, $\zeta = z/L$, and

$$\aleph = \frac{\pi d^2 \rho_c}{3\epsilon_0 \hbar \delta_L} \frac{L}{\lambda_L} \tag{46}$$

is a dimensionless parameter that describes the superradiant coupling between the incident and scattered fields. Equations (44) and (45), together with Eqs. (35) and (36), fully describe the multimode dynamics of the slowly varying envelopes of the electric and matter-wave fields. They may be solved analytically in the short-time regime as shown in the appendix. In this regime the fields $\Psi_{\pm k}$ obey

$$\Psi_k(\mathbf{r}, \tau) = \psi_{k'}(0) I_0(2\sqrt{\tau\Delta}), \tag{47}$$

where $\psi_{k'}(0)$ is the square root of the recoiling mode density at $\tau = 0$ and Δ is a function of ζ defined in the appendix. A similar result was previously obtained in Ref. [17].

IV. NUMERICAL RESULTS

A. General considerations

This section presents selected results from numerical simulations of the onset and growth of superradiant scattering in a cigar-shaped condensate. We assume here that all atoms in the condensate at temperature $T=0$ are initially in the electronic ground state $|1\rangle$, and approximate their center-of-mass wave function by a separable Thomas-Fermi profile (in dimensionless units),

$$\Psi_0(\mathcal{R}) = (6^{3/2} L^2/w^2) \prod_i \sqrt{(\mathcal{L}_i/2L)^2 - \mathcal{R}_i^2},$$

where the product is over the rescaled spatial coordinates $\mathcal{R}_i$ and $\mathcal{L}_i$ is the corresponding condensate width [26]. Close to the Thomas-Fermi radii, where the Thomas-Fermi approximation breaks down, we let the wave function go to zero smoothly by matching both the function and its derivative to a Gaussian tail. This is necessary to prevent numerical instabilities resulting from the advective term in Eq. (36). For comparison to the experiments of Ref. [1], we choose the aspect ratio of the condensate to be $w/L \approx 0.1$.

As we have seen, the amplitudes of the end-fire modes at the onset of the classical regime are stochastic variables, the values of which must be selected at random from run to run consistently with the results of Sec. II. However, to set the stage for our discussion, we consider first a simplified situation with only one left-recoiling and one right-recoiling side mode of equal initial amplitudes small compared to the amplitude of Ψ_0, but with the same spatial structure. We include, for the moment, only the atom-light coupling and neglect the mean-field interaction, the motion of the scattered atoms through the original condensate due to photon recoil, and dissipation.

Figure 3 shows the superradiant EFM pulse shape for several values of the atom-field coupling strength $\aleph$. To facilitate
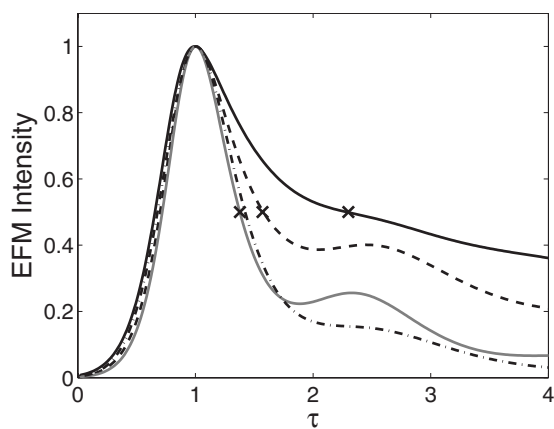
FIG. 3. Typical time evolution of the EFM intensity. These simulations neglect dissipation, mean-field interactions, and the motion of the scattered atoms through the condensate. The curves correspond to: solid line: $\aleph=6.0$, dashed line: $\aleph=3.0$; gray line: $\aleph=1.0$; and dot-dashed line, $\aleph=1.0$ with $\gamma/\delta_L=0.04$. The $\times$s mark points at which the spatial field and absorption profiles are plotted in Figs. 4–6.

comparison we scaled the peak intensities to 1, and the time axes so that the peaks coincide. The gray line, corresponding to $\aleph=1.0$, demonstrates a typical main pulse followed by a secondary peak, an effect known as ringing [2]. Increasing the coupling strength to $\aleph=3.0$ raises the secondary peak maximum relative to the first peak, as shown by the dashed line. The black line, for which $\aleph=6.0$, represents a qualitatively different regime: The superradiant maximum is now followed by a slowly decaying tail rather than ringing. Dissipation also leads to suppression of the ringing, as shown by the dot-dashed line, which is for $\gamma/\delta_L=0.04$ and $\aleph=1.0$. The appearance of ringing with increased coupling strength has been observed experimentally [Fig. 3(b) of Ref. [4]].

Figures 4 and 5 show spatial profiles along the long axis z of the condensate, of the atomic side mode Ψ_{+k}, and of the corresponding EFM field $\mathcal{E}_{-k}$. Here the same values of $\aleph$ as
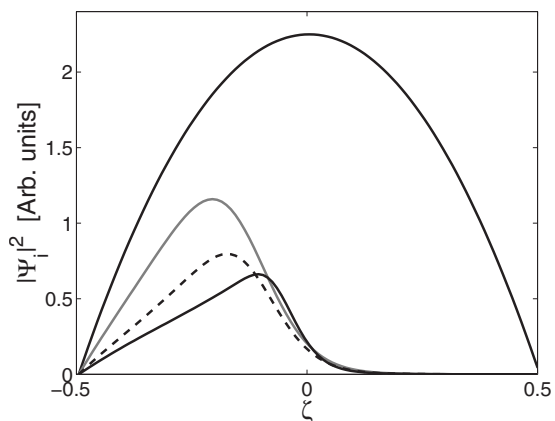
FIG. 4. Density profile of the condensate at $\tau=0$ (top solid line) and of the atomic side mode Ψ_{+k} at half the maximum EFM intensity, as indicated by $\times$s in Fig. 3. Solid line: $\aleph=6.0$; dashed line: $\aleph=3.0$; and gray line: $\aleph=1.0$. Mean-field interactions, dissipation, and the motion of the scattered atoms through the condensate are neglected.
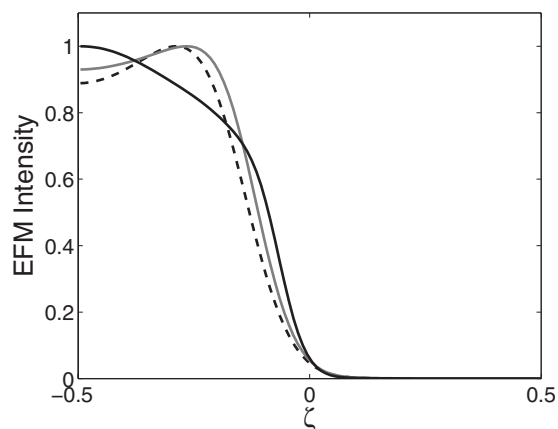
FIG. 5. Typical spatial envelopes of EFM electric fields at half maximum EFM intensity as indicated by $\times$s in Fig. 3. Solid line: $\aleph=6.0$; dashed line: $\aleph=3.0$; gray line: $\aleph=1.0$. The peak in intensity for $\aleph=1.0$ and 3.0 arises due to the scattering of EFM photons back into the probe beam. Mean-field interactions, dissipation, and the motion of the scattered atoms through the original condensate are neglected here.

in Fig. 3 were used; solid line: $\aleph=6.0$; dashed line: $\aleph=3.0$; and gray line: $\aleph=1.0$. The EFM profiles have again been scaled for comparison. All z-axis profiles correspond to the times indicated by the $\times$s in Fig. 3. In Fig. 4 the atomic mode Ψ_{+k} grows from the left edge of $|\Psi_0|(\zeta)^2$, a consequence of the buildup of the EFM electric field as it moves across the condensate (see Fig. 5). For clarity the mode Ψ_{-k} is not shown. It is simply a mirror image of Ψ_{+k}. Interestingly, in the absence of dissipation the weaker coupling strength is more efficient at scattering atoms to the ground state $|2\rangle$ over a single superradiant pulse, as evidenced by the gray line in Fig. 4. Keep in mind, however, that the time scale is slower for the weaker coupling, a feature not apparent due to the scaling of time in the figure.

For the cases $\aleph=1.0$ and 3.0, the EFM profile peaks before reaching the edge of the condensate (see Fig. 5). During the dynamical evolution this peak appears shortly after the first intensity maximum in Fig. 3. It is a consequence of the EFM field being scattered back into the probe beam from atoms in ground state $|2\rangle$. As pointed out in Ref. [17] this may cause a strong EFM field to exist within the atomic system despite small emission outside the sample.

The fraction of absorbed laser intensity

$$A(x,z) = \frac{|\mathcal{E}_L^{\text{in}}|^2 - |\mathcal{E}_L(x,z)|^2}{|\mathcal{E}_L^{\text{in}}|^2} \tag{48}$$

is shown in Fig. 6 for $x \gg w$ after the laser field exits the condensate, again for the same values of $\aleph$ as in Fig. 3 and at half the EFM intensity maximum. The two central peaks in each absorption profile appear close to the edges of the condensate early in the time evolution and then migrate towards each other. Secondary features, such as regions of gain around the edges of the condensate, appear shortly after the EFM pulse maximum for $\aleph=1.0$ and 3.0. This indicates that EFM light is being scattered back into the pump field. For $\aleph=6.0$ the growth of secondary absorption peaks at the edges
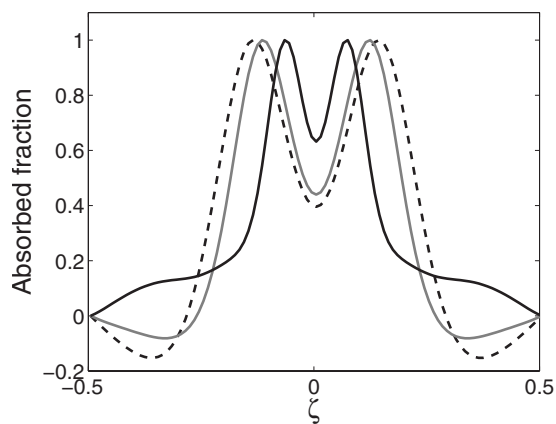
FIG. 6. Absorption profile of the pump pulse along the z axis at half maximum EFM intensity as indicated by $\times$s in Fig. 3. Solid line: $\aleph=6.0$; dashed line: $\aleph=3.0$; and gray line: $\aleph=1.0$. Mean-field interactions, dissipation, and the motion of the scattered atoms through the original condensate are neglected here.

of the condensate, as shown by the black line, is the dominant secondary feature rather than gain.

The semiclassical model is valid provided the relevant modes are macroscopically occupied. In the above simulations the initial seed amplitude of the recoiling atomic modes was treated as a free parameter that may in general be chosen to fit experimental data. To study the effects of this choice of initial amplitude we plot in Fig. 7 the time evolution of EFM intensity for initial densities of the recoiling modes being, respectively, 10^{-6} (solid black line), 10^{-5} (dashed line), and 10^{-4} (gray line) times smaller than the condensate density. For smaller initial amplitude the time-to-peak superradiance is delayed and the ringing peak is higher relative to the intensity maximum.

Now consider the effects of mean-field interactions and the motion of the scattered atoms through the original condensate. Figure 8 shows the time evolution of the EFM intensity for $\gamma/\delta_L=8\times10^{-3}$ and $\aleph=1.7$. The results are for simulations taking into account superradiance only (solid black line), superradiance and recoil velocity (dashed line), superradiance and mean-field interaction (dot-dashed line),
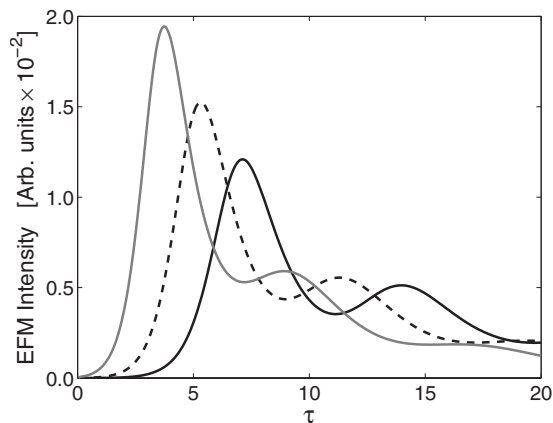
FIG. 7. Time evolution of EFM intensity for an initial density of the recoiling modes 10^{-6} (solid black line), 10^{-5} (dashed line), and 10^{-4} (gray line) times smaller than the condensate density.
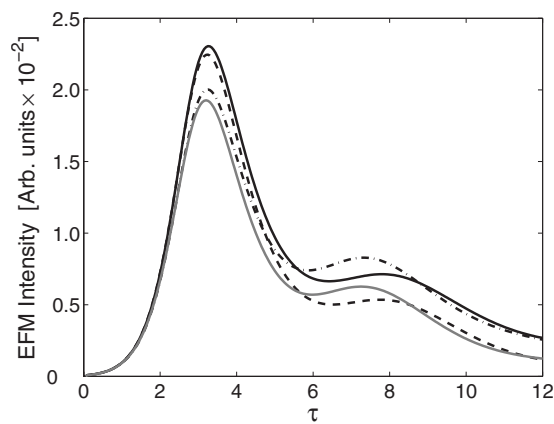
FIG. 8. Comparison of EFM intensity with $\gamma/\delta_L=8\times10^{-3}$, $\aleph=1.7$ for superradiance only (black solid line), superradiance and recoil velocity of the scattered atoms (dashed line), superradiance and mean-field interaction (dot-dashed line), and superradiance with both mean-field interactions and atomic recoil velocity included (gray line).

and superradiance with both mean-field interactions and recoil velocity (gray line). The recoil velocity was so chosen that an atom would traverse roughly half a condensate width over $\Delta\tau=12.0$. The primary effect of including the photon recoil and mean-field interactions is to reduce the EFM amplitude. Note that the height of the ringing peak is increased somewhat relative to the first intensity maximum when including only mean-field interactions. But generally speaking we do not find significant qualitative changes in the spatial and temporal evolution of either matter or light fields other than a reduction in overall amplitudes and slight relative delays.

B. Comparison with experiment

The primary purpose of the multimode treatment is to describe the quantum fluctuations that govern the initial evolution of the system. As discussed in Sec. II, this entails randomly choosing seed amplitudes for the initial state of the recoiling atomic modes with the appropriate statistical properties. We have found, however, that the multimode description gives the same results as a single-mode model as far as EFM intensity and absorption profiles are concerned, provided that the sum of initial seed densities in the multimode case is equal to the seed density of the single-mode system. For a single run of the experiment a single-mode description is therefore sufficient if the seed densities are chosen judiciously. We thus turn to a comparison of the single-mode theory to data obtained in experiments at UC Berkeley [24].

As described in Ref. [1], a Bose condensate of $N=1.6\times10^6$ ^{87}Rb atoms trapped in an Ioffe-Pritchard trap with trap frequencies of $\omega_{x,y,z}=2\pi(48,48,5)s^{-1}$ was superradiantly pumped via the $F=1\rightarrow F'=1$ D1 transition from the $|F=1,m_f=-1\rangle$ to the $|F=2,m_f=1\rangle$ ground states via a sequence of ten pump pulses of 100 μs, each separated by a 68 μs delay. (This delay is important for studies at nonzero temperatures, since it allows the noncondensed atoms to dephase, thus keeping the experiment sensitive to the con-
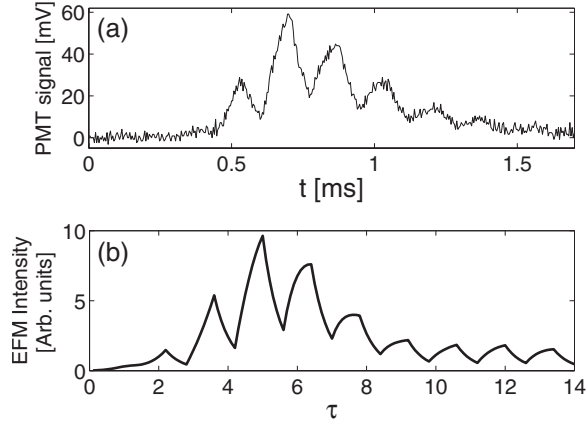
FIG. 9. Comparison between (a) the experimental photomultiplier signal of EFM intensity [1] and (b) the theoretical prediction for $\aleph = 1.7$. Experimental data by Stamper-Kurn *et al.* [24].

densed fraction only. It is, however, unimportant in the present zero-temperature theory.) For these experimental parameters and an *s*-wave scattering length for ^{87}Rb of $a \approx 100a_0$, the condensate has an aspect ratio of about $w/L \approx 0.1$ and $\aleph \approx 1.7$.

Figure 9(a) shows a typical EFM pulse sequence recorded on a photomultiplier tube (PMT). The rise time between pulses is a consequence of the slow response time of the PMT. The lack of ringing indicates that dissipation plays a significant role in the dynamics. Dissipation due to spontaneous emission may be estimated using $\gamma/\delta_L = \omega^3 d^2/3\pi\epsilon_0\hbar c^3\delta_L \approx 8 \times 10^{-3}$ [25]. The experimental data agree qualitatively with the three-dimensional simulation [see Fig. 9(b)]. Here the initial density of recoiling atoms was chosen 10^4 times smaller than the condensate density, and the dimensionless time scale was such that an atom would traverse roughly half a condensate width over the course of the pulse sequence as in the Berkeley experiments. The PMT response was accounted for by convoluting the EFM intensity with a response function with response time of the order of the pulse separation.

Experimental absorption images corresponding to the PMT signal of Fig. 9(a) are shown in Fig. 10(a), where time evolves from top to bottom and each image is the time-averaged absorption over the duration of each pulse in the sequence. Consistently with the observation that in this experimental run the asymmetry in the absorption profile is small, we have taken the initial amplitudes of the atomic-side modes $\Psi_{\pm k}$ to be equal. The resulting theoretical absorption images are shown in Fig. 10(b). An effect not resolved in Ref. [1] is the weak absorption seen at the outer edges along the radial direction of the condensate in the lower six images of Fig. 10(b). This absorption arises since the condensate is less dense there than in the center, thus delaying the superradiance in time and intensity. A comparison between the theory and transversely averaged experimental absorption profiles is shown in Fig. 10(c). The qualitative agreement is quite satisfactory although the value of the peak absorption is underestimated by a factor of ∼2. Note that the averaging procedure suppresses gain and other secondary features seen in the simulation of Fig. 10(b), thus leading to the simple

double-peaked structure of Fig. 10(c). The simulation furthermore suggests that these features are too small in spatial extent and amplitude to be resolved in the experimental data.

The only free parameters in this simulation are the initial seed amplitude and the total time duration of the pulse sequence, and they are tightly constrained by, respectively, the rise time to peak superradiance relative to the EFM pulse width and the EFM pulse width relative to the overall time duration of the pulse sequence. Nonetheless, an alternative approach to comparing theory and experiment would be to adjust $\aleph$ to produce a best fit. We have also used such an approach, leading to the value $\aleph_{\text{bestfit}} \approx 3.5$, a value that removes the factor-of-2 discrepancy mentioned earlier, but at the cost of overestimating the particle number in the sample by the same factor.

C. Shot-to-shot fluctuations

We now turn to the shot-to-shot fluctuations resulting from the quantum noise-dominated early stages of the emission process. In Fig. 11(a) we show a typical absorption image obtained experimentally and exhibiting strong asymmetry, as well as its transverse averaged profile in Fig. 11(b). To account for this asymmetry we solve the multimode Eqs. (35) and (36) and Eqs. (44) and (45) for $\aleph = 3.0$, neglecting mean-field interactions and effects due to the motion of the scattered atoms, with the initial amplitude of each quasimode chosen from the probability distribution (23) independently of the other modes. The average particle number $\bar{n}_{\mathbf{q}}$ is taken to be the same for all distributions.

Figures 12(a) and 12(b) show absorption profiles for two randomly chosen realizations of a superradiance experiment for systems with (a) $m=5$ and (b) $m=20$ quasimodes each in the left and right EFM directions of propagation. In all cases the absorption profile is shown at the time of the first EFM intensity maximum in either the left- or right-traveling EFM. The separation ΔA, as indicated by the dotted lines in Fig. 12(a), may be used to characterize the asymmetry. Figures 12(c) and 12(d) shows a gray-scale plot constructed from 500 realizations of the superradiance experiment for (c) $m=5$ and (d) $m=20$ quasimodes each in the left- and right-traveling EFMs. Each profile is again taken at the first EFM intensity maximum. The gray scale represents the frequency of occurrence of absorption, with the darkest shade of gray being the highest frequency.

The distribution of absorption asymmetries ΔA for a random set of 500 realizations of the experiment is plotted in Fig. 12(e) for $m=5$ (black line), $m=10$ (gray line), and $m=20$ (dashed line) quasimodes each in the left- and right-EFM directions. As may be expected the width of the distribution decreases with increasing number of modes.

V. CONCLUSION

We have presented a multimode theory of Raman superradiance scattering that includes both its initiation from quantum noise and its full time dependence while the pump laser propagates through the condensate. Superradiant Raman scattering into end-fire modes leads to nontrivial, time-
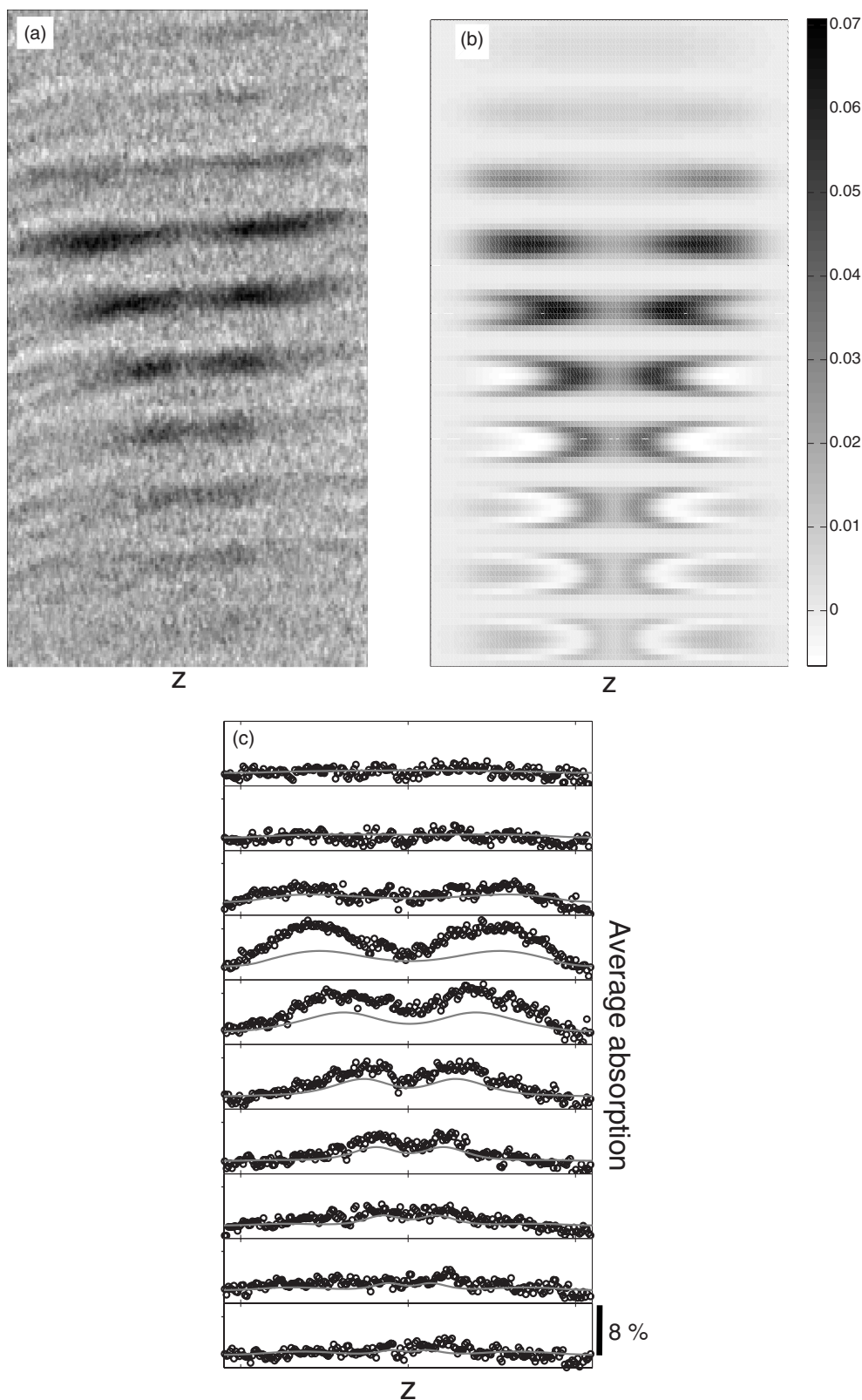
FIG. 10. (a) Experimental coherent-absorption imaging data [1], where the darkest regions indicate the strongest absorption, with a maximum absorption of ~15%. (b) Theoretical absorption images for $\aleph = 1.7$ and an initial density of recoiling modes $|\Psi_0|^2/10^4$. (c) Comparison between experimental (circles) and theoretical (gray lines) transverse averaged absorption profiles. The maximum in the experimental data is ~6%. In all figures time evolves from top to bottom and the horizontal frame width is $L \approx 200$ μm. Experimental data by Stamper-Kurn *et al.* [24].
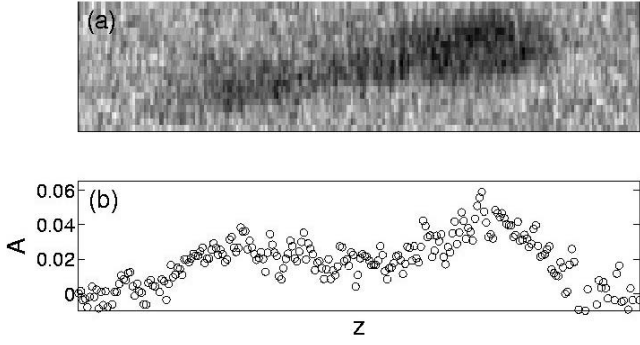
FIG. 11. Example of (a) typical absorption image (see Ref. [1]), and (b) its averaged profile, demonstrating the asymmetry that typically arises from quantum fluctuations. Experimental data by Stamper-Kurn *et al.* [24].

dependent, spatial structures in both the matter and optical fields. The microscopic quantum fluctuations that trigger the initial superradiant dynamics lead to macroscopic fluctuations and asymmetries in the spatial features of absorption images during later stages. This theory successfully explains the main dynamical features of recent experiments that exploit it as an imaging tool for quantum-degenerate atomic systems, the calculated absorption profiles being in good qualitative agreement with experimental observations. Future work will extend this theory to finite temperatures and to the case of fermionic systems.

ACKNOWLEDGMENTS

APPENDIX

The short-time expressions may be obtained by ignoring the depletion for the laser field, $\mathcal{E}_L \approx 1$, and keeping only highest-order terms in the equations of motion for the atomic fields and end-fire modes,

$$\frac{d\Psi_0(\mathbf{r},t)}{d\tau} \approx \frac{i}{(1-i\gamma/\delta)}|\mathcal{E}_L|^2\Psi_0, \tag{A1}$$

$$\frac{d\Psi\mathbf{k}(\mathbf{r},t)}{d\tau} \approx \frac{i}{(1-i\gamma/\delta)}\mathcal{E}^*_{-\mathbf{k}}\mathcal{E}_L\Psi_0, \tag{A2}$$

$$\text{sgn}(k)\frac{\partial\mathcal{E}_k}{\partial\zeta} \approx \frac{i\aleph}{(1-i\gamma/\delta)}\Psi^\dagger_{-k}\mathcal{E}_L\Psi_0. \tag{A3}$$

Equation (A1) may immediately be solved to give

$$\Psi_0(\tau) = \Psi_0^{(0)}e^{i\eta\tau}e^{-\nu\tau}, \tag{A4}$$

where $\eta = \frac{1}{[1+(\gamma/\delta)^2]}$, $\nu = \frac{\gamma/\delta}{[1+(\gamma/\delta)^2]}$, and $\Psi_0^{(0)}$ is the initial condensate wave function, which is assumed to be of the form $\Psi_0^{(0)} = \phi_\zeta\phi_{(\xi,Y)}$. Here $Y=y/L$ is the dimensionless length in the y direction. We also assume that in the initial state the recoiling atomic modes have the same wave function as the condensate, but smaller in amplitude by a factor $\beta \ll 1$. At time $\tau=0$ the EFM field is, by direct integration of Eq. (A3),

$$\text{sgn}(k)\mathcal{E}_k(\zeta) = \aleph(i\eta-\nu)\beta|\phi_{(\xi,Y)}|^2\left(\int_{-1/2}^\zeta |\phi_{\zeta'}|^2 d\zeta' + \mathcal{E}_0\right)$$

$$= \aleph(i\eta-\nu)\beta|\phi_{(\xi,Y)}|^2\Delta(\zeta)/\alpha, \tag{A5}$$

where $\mathcal{E}_0$ is chosen so that the boundary condition $\mathcal{E}_{-k}(1/2)=0$ is satisfied and

$$\Delta(\zeta) = \alpha\left(\int_{-1/2}^\zeta |\phi_\zeta|^2 d\zeta' + \mathcal{E}_0\right), \tag{A6}$$

where
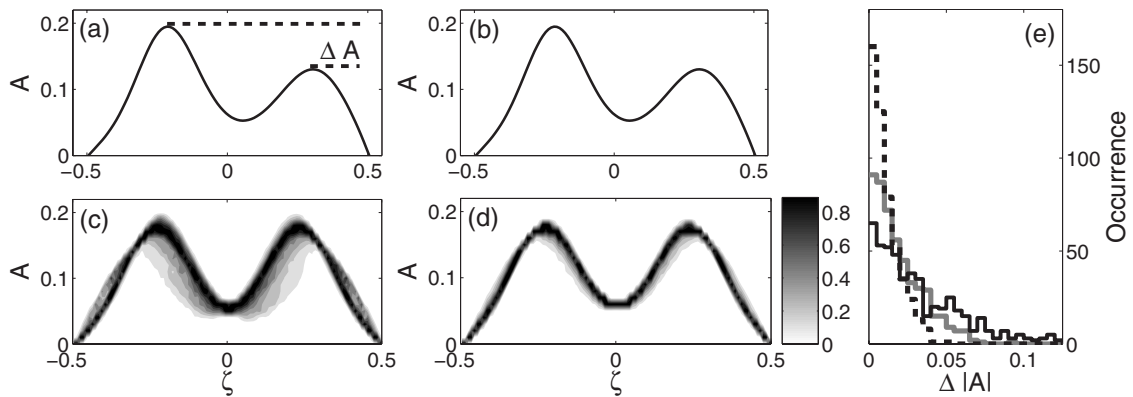
FIG. 12. Absorption profile $A(\zeta)$ of the input laser field. Figures (a) and (b) are representative profiles resulting from single realizations of a superradiance experiment for geometries with (a) $m=5$ and (b) $m=20$ quasimodes each in the left and right EFM directions. The peak separation ΔA as indicated by the dotted lines in (a) characterizes the asymmetry. Figures (c) and (d) give the frequency of occurrence of the absorption profiles resulting from 500 realizations for (c) $m=5$ and (d) $m=20$. As indicated by the gray scale in the color bar, the darkest shade of gray corresponds to the most frequent occurrences. (e) Distribution of the asymmetry of absorption peaks from 500 realizations, for systems with $m=5$ (black line), $m=10$ (gray line), and $m=20$ (dashed line) quasimodes in both the left and right EFM directions.

$$\alpha = \frac{\aleph}{[(1 + (\gamma/\delta)^2\,]}|\phi_{\xi,Y}|^2. \tag{A7}$$

Now substitute Eq. (A4) into Eq. (A3) and define $\widetilde{\mathcal{E}}^*_{-k} = \mathcal{E}^*_{-k}e^{i\eta\tau+\nu\tau}$. Then upon taking the time derivative of Eq. (A3) and the substitution of Eq. (A2) we find

$$\text{sgn}(k)\frac{\partial^2 \widetilde{\mathcal{E}}^*_{-k}}{\partial\tau\partial\zeta} = \alpha|\phi_\zeta|^2\widetilde{\mathcal{E}}^*_{-k}e^{-2\nu\tau}. \tag{A8}$$

We first treat the case of zero dissipation, i.e., $\eta \to 1$ and $\nu \to 0$. Taking the Laplace transform of Eq. (A8) with respect to time we obtain

$$s\frac{\mathsf{E}^*_{-k}(\zeta,s)}{\partial\zeta} - i\aleph\beta|\Psi_0^{(0)}|^2 = \alpha|\phi_\zeta|^2\mathsf{E}^*_{-k}(\zeta,s), \tag{A9}$$

in which $\mathsf{E}^*_{-k}(\zeta,s) = \mathcal{L}(\widetilde{\mathcal{E}}^*_{-k})$. Equation (A9) is a linear first-order differential equation that may be solved by standard means. We find

$$\mathsf{E}^*_{-k}(\zeta,s) = be^{\Delta(\zeta)/s} - i\aleph\beta|\phi_{(\xi,Y)}|^2/\alpha. \tag{A10}$$

The EFM field is found by the inversion of the Laplace transform

$$\mathcal{E}^*_{-k}(\zeta,\tau) = \frac{1}{2\pi i}\int_{\mu-i\infty}^{\mu+i\infty} e^{s\tau}\mathsf{E}^*_{-k}(\zeta,s)ds. \tag{A11}$$

The contour of integration is chosen so as to include all poles of the integrand and the integral may be evaluated using the residue theorem. This is done by expanding both exponentials in the integrand in series and multiplying out the result. Integrating term by term the residue is found to be of the form

$$\sum_{n=1}^\infty \frac{\tau^{n-1}\Delta^n}{(n-1)!n!} = \sqrt{\frac{\Delta}{t}}I_1(2\sqrt{\tau\Delta}), \tag{A12}$$

where I_q is a modified Bessel function of the first kind of order q. Thus

$$\mathcal{E}^*_{-k}(\zeta,\tau) = i\beta\sqrt{\frac{\Delta}{\tau}}I_1\,(2\sqrt{\tau\Delta})|_{u=0}, \tag{A13}$$

and by substitution into Eq. (A3)

$$\Psi_{\mathbf{k}}(\mathbf{r},\tau) = \beta\Psi_0^{(0)}I_0\,(2\sqrt{\tau\Delta})|_{\nu=0}. \tag{A14}$$

We now turn to the case of nonzero dissipation. Since the solution to the latter must reduce to Eq. (A13) for $\nu \to 0$, we try a solution of the form

$$\mathcal{E}^*_{-k} \sim a_1(\tau)\Delta + a_2(\tau)\Delta^2 + a_3(\tau)\Delta^3 + \cdots \tag{A15}$$

where the $a_n(\tau)$ are time-dependent coefficients that must vanish at $\tau=0$ and reduce to $\tau^{n-1}/(n-1)!n!$ for $\nu \to 0$. Substituting Eq. (A15) into Eq. (A8) one obtains a recursion relation for the nth coefficient

$$\frac{\partial a_n}{\partial\tau} = \frac{a_{n-1}}{n}e^{-2\nu\tau}. \tag{A16}$$

To satisfy the $\nu \to 0$ condition we find that

$$a_n = \frac{1}{2^{n-1}\nu^{n-1}(n-1)!n!}(1 - e^{-2\nu\tau}), \tag{A17}$$

leading to the desired solution

$$\widetilde{\mathcal{E}}^*_{-k}(\mathbf{r},\tau) = i\beta(1 - i\gamma/\delta)\left(\frac{2\nu\Delta(\zeta)}{1 - e^{-2\nu\tau}}\right)^{1/2}I_1(g(\zeta)), \tag{A18}$$

and

$$\Psi_k(\mathbf{r},\tau) = \beta\Psi_0^{(0)}I_0(g(\zeta)). \tag{A19}$$

The argument of the Bessel functions is given by

$$g(\zeta) = \left(\frac{2\Delta(\zeta)(1 - e^{-2\nu\tau})}{\nu}\right)^{1/2}. \tag{A20}$$

Finally, to find the absorption profiles of the laser field we have to include all terms in the differential equation

$$\frac{\partial\mathcal{E}_L}{\partial\xi} = \frac{i\aleph}{(1 - i\gamma/\delta)}\Psi_0^\dagger\left\{\mathcal{E}_L\Psi_0 + \sum_k \mathcal{E}_k\Psi_{-k}\right\}. \tag{A21}$$

For simplicity we take a uniform distribution in the ξ direction since the exact ξ profile should not be too important in the short time limit. Substituting the short-time solutions obtained above we find

$$\mathcal{E}_L(\zeta) = e^{f(\zeta)} - \sum_{\sigma=\pm 1}\aleph\beta|\Psi_0^{(0)}|^2\frac{(1 + i\gamma/\delta)}{(1 - i\gamma/\delta)}\frac{2\Delta(\zeta)}{g(\sigma\zeta)}I_1(g(\sigma\zeta))$$

$$\times I_0(g(\sigma\zeta))\frac{e^{f(\zeta)} - 1}{f(\zeta)}, \tag{A22}$$

where

$$f(\zeta) = \aleph(i\eta - \nu)\phi_\zeta\int_{-(w/2L)}^{w/2L}\phi_{(\xi,Y)}d\xi. \tag{A23}$$

For a Thomas-Fermi profile $\phi_\zeta = \sqrt{(1/2)^2 - \zeta^2}$ and

$$\Delta(\zeta) = \alpha\left(\frac{2}{3}(1/2)^3 - (1/2)^2\zeta + \frac{1}{3}\zeta^3\right). \tag{A24}$$

---

[1] L. E. Sadler, J. M. Higbie, S. R. Leslie, M. Vengalattore, and D. M. Stamper-Kurn, Phys. Rev. Lett.(to be published).
[2] M. Gross and S. Haroche, Phys. Rep. **93**, 301 (1982).
[3] R. H. Dicke, Phys. Rev. **93**, 99 (1954).
[4] S. Inouye, A. P. Chikkatur, D. M. Stamper-Kurn, J. Stenger, D.
E. Pritchard, and W. Ketterle, Science **285**, 571 (1999).
[5] S. Inouye, T. Pfau, S. Gupta, A. P. Chikkatur, A. Görlitz, D. E. Pritchard, and W. Ketterle, Nature (London) **402**, 641 (1999).
[6] D. Schneble, Y. Torii, M. Boyd, E. W. Streed, D. E. Pritchard, and W. Ketterle, Science **300**, 475 (2003).

[7] D. Schneble, K. C. Gretchen, W. S. Erik, B. Micah, D. E. Pritchard, and W. Ketterle, Phys. Rev. A **69**, 041601(R) (2004).

[8] Y. Yoshikawa, T. Sugiura, Y. Torii, and T. Kuga, Phys. Rev. A **69**, 041603(R) (2004).

[9] K. V. Krutitsky, F. Burgbacher, and J. Audretsch, Phys. Rev. A **59**, 1517 (1999).

[10] M. G. Moore and P. Meystre, Phys. Rev. Lett. **83**, 5202 (1999).

[11] O. E. Müstecaplioglu and L. You, Phys. Rev. A **62**, 063615 (2000).

[12] M. M. Cola and N. Piovella, Phys. Rev. A **70**, 045601 (2004).

[13] F. Arecchi and E. Courtens, Phys. Rev. A **2**, 1730 (1970).

[14] R. Bonifacio, P. Schwendimann, and F. Haake, Phys. Rev. A **4**, 302 (1971).

[15] R. Bonifacio and L. Lugiato, Phys. Rev. A **11**, 1507 (1975).

[16] O. Zobay and G. M. Nikolopoulos, Phys. Rev. A **72**, 041604(R) (2005).

[17] O. Zobay and G. M. Nikolopoulos, Phys. Rev. A **73**, 013620 (2006).

[18] F. A. Hopf and P. Meystre, Phys. Rev. A **12**, 2534 (1975).

[19] F. A. Hopf, P. Meystre, and D. W. McLaughlin, Phys. Rev. A **13**, 777 (1976).

[20] F. Haake, J. W. Haus, H. King, G. Schröder, and R. Glauber, Phys. Rev. A **23**, 1322 (1981).

[21] I. E. Antoniou, V. V. Kocharovsky, V. L. V. Kocharovsky, Y. M. Mironov, and I. A. Shereshevsky, Comput. Math. Appl. **34**, 751 (1997).

[22] F. E. van Dorsselaer and G. Nienhuis, Phys. Rev. A **56**, 958 (1997).

[23] Y. B. Band, M. Trippenbach, J. P. Burke, Jr., and P. S. Julienne, Phys. Rev. Lett. **84**, 5462 (2000).

[24] D. M. Stamper-Kurn, L. E. Sadler, and M. Vengalattore (private communication).

[25] H. Metcalf and P. van der Straten, *Laser Cooling and Trapping* (Springer-Verlag, New York, 2002).

[26] Around the center of the wave function this approximation has small corrections, second order in $x_i x_j / r_i r_j$, to the true Thomas-Fermi wave function.